

Search with EGRET for a Gamma Ray Line from the Galactic Center

Anthony R. Pullen, Ranga-Ram Chary, and Marc Kamionkowski
California Institute of Technology, Mail Code 130-33, Pasadena, CA 91125

(Dated: December 2, 2024)

We search data from the Energetic Gamma Ray Experiment Telescope (EGRET) for a gamma-ray line in the energy range 0.1–10 GeV from the $10^\circ \times 10^\circ$ region around the Galactic center. Our null results lead to upper limits to the line flux from the Galactic center. Such lines may have appeared if the dark matter in the Galactic halo is composed of weakly-interacting massive particles (WIMPs) in the mass range 0.1–10 GeV. For a given dark-matter-halo model, our null search translates to upper limits to the WIMP two-photon annihilation cross section as a function of WIMP mass. We show that for a toy model in which Majorana WIMPs in this mass range annihilate only to electron-positron pairs, these upper limits supersede those derived from measurements of the 511-keV line and continuum photons from internal bremsstrahlung at the Galactic center.

PACS numbers: 95.85.Pw, 95.35.+d, 98.35.Gi

I. INTRODUCTION

Weakly-interacting massive particles (WIMPs) provide promising candidates for the dark matter in Galactic halos [1, 2, 3]. The most deeply explored WIMP candidate is the neutralino, the lightest superpartner in many supersymmetric extensions of the standard model [4]. Although the favored mass range for neutralinos is usually $\gtrsim 10$ GeV, there are other WIMP candidates with masses in the 0.1–10 GeV range. For example, neutralinos with masses as low as 6 GeV are plausible if gaugino unification is not assumed [5]. Neutralinos with masses as low as 100 MeV are plausible in the next-to-minimal supersymmetric standard model (NMSSM) [6, 7]. Also, scalar and spin-1/2 particles with masses in the MeV range have been considered [8] to explain the 511-keV gamma-ray line observed by INTEGRAL.

One way to detect WIMPs is to search for monoenergetic gamma rays, with energies equal to the WIMP mass m_χ , produced by pair annihilation of WIMPs in the Galactic halo [9]. Such a line spectrum could be easily distinguished from the continuum spectrum from more prosaic gamma-ray sources (e.g., cosmic-ray spallation), and thus serve as a “smoking gun” for dark-matter annihilation.

Since the dark-matter density is highest at the Galactic center, the flux of WIMP-annihilation photons should be greatest from that direction. On the other hand, the continuum background should also be highest from the Galactic center. We estimate that for a Navarro-Frenk-White profile [10], the WIMP-annihilation flux from the $10^\circ \times 10^\circ$ region from the Galactic center should exceed that from the Galactic anticenter by a factor ~ 100 , while the flux of cosmic-ray-induced photons at energies $O(\text{GeV})$ is only about 8 times higher from the Galactic center than from the Galactic anticenter. Thus, the Galactic center is the preferred place to look for a WIMP-annihilation signal. It is also the location of the 511-keV anomaly that has motivated the consideration of lower-mass WIMPs.

In this paper, we search data from the Energetic

Gamma Ray Experiment Telescope (EGRET) [11] on the Compton Gamma Ray Observatory (CGRO) for a gamma-ray line in the energy range 100 MeV to 10 GeV from a $10^\circ \times 10^\circ$ region around the Galactic center. We found no evidence for a gamma-ray line from the Galactic center in this energy range. From these null results, we can bound the cross section $\langle\sigma v\rangle_{\gamma\gamma}$ for WIMP annihilation to two photons for WIMPs in this mass range.

The plan of our paper is as follows: In Section II, we discuss how EGRET data are cataloged. In Section III, we reconstruct from the EGRET data the differential flux of photons as a function of energy. In Section IV, we fit to the data a model of the flux produced by cosmic rays and point sources near the Galactic center. In Section V, we search for a line excess of photons from WIMP annihilation. In Section VI, we report upper limits to $\langle\sigma v\rangle_{\gamma\gamma}$ as a function of m_χ for WIMPs within the mass range of 0.1 GeV to 10 GeV for a variety of dark-matter-halo models. In Section VII, we show that in a toy model in which the WIMP annihilates only to electron-positron pairs, this upper limit is stronger over this mass range than limits derived from the 511-keV line and from lower-energy continuum gamma rays from internal bremsstrahlung.

II. SOURCE OF DATA

We obtained publicly available data from the CGRO Science Support Center (COSSC).¹ We used the EGRET photon lists (QVP files), which contain event lists of all photons detected during a given viewing period. The data that we used from these files are the photon’s Galactic latitude, Galactic longitude, zenith, energy, and energy uncertainty. We also required the exposure files, which contain the detector’s effective area multiplied by the viewing time of the detector for a particular viewing period multiplied by EGRET’s 1-sr field of view.

¹ <http://cosscc.gsfc.nasa.gov/docs/cgro/cosscc/egret/>

TABLE I: Energy range for each energy bin.

Energy Bin	Energy Range (MeV)	Half-Bin Size (MeV)
1	30–50	10
2	50–70	10
3	70–100	15
4	100–150	25
5	150–300	75
6	300–500	100
7	500–1000	250
8	1000–2000	500
9	2000–4000	1000
10	4000–10000	3000

TABLE II: Viewing periods used in analysis.

5.0	7.2	13.1	16.0	20.0	23.0	24.0	24.5
25.0	27.0	35.0	38.0	42.0	43.0	207.0	209.0
210.0	214.0	217.0	219.0	223.0	226.0	229.0	229.5
231.0	232.0	302.3	323.0	324.0	330.0	332.0	334.0
336.5	339.0	403.0	421.0	422.0	423.0	423.5	429.0

The exposure is provided as a function of latitude, longitude, and energy range. We also obtained the counts files, which contain the number of photons at various spatial coordinates and energy ranges within a viewing period. The energy bins, along with their respective energy ranges, are listed in Table I. Also listed in Table I are the half-bin sizes.

III. CONSTRUCTION OF GAMMA RAY FLUX

We begin by constructing the photon differential flux as a function of energy. We use data only from a square region on the sky centered at the Galactic center from -5° to 5° Galactic longitude and -5° to 5° Galactic latitude. Each viewing period covers a particular region of the sky, and there were 40 viewing periods for our region of interest. These viewing periods were found using Table 1 in the Third EGRET Catalog [12]. We list the viewing periods used in Table II.

We split the data into 119 energy bins, with each bin ranging in energy from $E_{\min,i} = 30 \times 1.05^i$ MeV to $E_{\max,i} = 30 \times 1.05^{i+1}$ MeV, where i ranges from 0 to 118. Since the photon index for the photon distribution is 2.1, the average energy E_{avg} of photons in an energy bin $[E_{\min}, E_{\max}]$ is

$$E_{\text{avg}} = 11 \times \frac{E_{\min}^{-0.1} - E_{\max}^{-0.1}}{E_{\min}^{-1.1} - E_{\max}^{-1.1}} \text{ MeV}. \quad (1)$$

The counts files can be used to calculate the number of photons in each of the ten large bins listed in Table I, from which the differential flux for each large bin can be calculated. We also confirmed that the fluxes we calculate from the events files are compatible with the fluxes

from the counts files, which is the most commonly used EGRET data product.

With these quantities, we calculate the differential flux (photons $\text{cm}^{-2} \text{s}^{-1} \text{sr}^{-1} \text{MeV}^{-1}$),

$$F(E_i) = \frac{n(E_i)}{\varepsilon(E_i)\Delta E_i}, \quad (2)$$

where E_i is the average energy of one of the ten large energy bins in Table I, $n(E_i)$ is the number of photons within that energy bin, $\varepsilon(E_i)$ is the total exposure over the viewing region within that energy bin, and ΔE_i is the size of the energy bin. The quantities $n(E_i)$ and $\varepsilon(E_i)$ are both summed over all viewing periods and all positions within the region of interest. The uncertainty $\sigma_F(E_i)$ in the flux is

$$\sigma_F(E_i) = \frac{\sqrt{n(E_i)}}{\varepsilon(E_i)\Delta E_i}. \quad (3)$$

We assume Gaussian errors in the photon energy. The uncertainty in energy is calculated differently for the counts data than for the events data. For the counts data, the energy uncertainty equals half the bin size, as shown in Table I. For the events data, the energy uncertainty is just the median of the energy uncertainties of the individual photons within that energy bin. The small energy bins in our final flux are much smaller than the energy uncertainty of the instrument. This is taken into account in the analysis described in Section V. We constructed two estimates of the differential flux. In one estimate we used the counts files to calculate $n(E_i)$, while in the other estimate we used the events files to calculate $n(E_i)$. Results are shown in Fig. 1.

In order to reproduce the counts data from the events file, we must reject photons with zenith angles greater than 100° and energy uncertainties greater than 40% of the photon energy. We are not able to match the two fluxes at the first energy bin to within 25%. However, for reasons discussed below, we discard energy bins below 0.1 GeV from our analysis.

Applying the same photon rejections, we construct a differential flux with 119 energy bins. To calculate exposures, we interpolate $\log[\varepsilon(E_n)]$ over $\log(E_n)$, where E_n is an average energy for a large energy bin n , and $\varepsilon(E_n)$ is the same exposure for the large bin n used for the ten large bins earlier. The flux along with the flux uncertainty is shown in Fig. 2. Figs. 1 and 2 agree with EGRET's measurement of the diffuse gamma-ray spectrum in the same region of sky, shown in Fig. 4 of Ref. [13].

IV. DETERMINATION OF FLUCTUATIONS OF GAMMA-RAY FLUX

We consider five traditional astrophysical sources for the diffuse gamma-ray background from the Galaxy. In

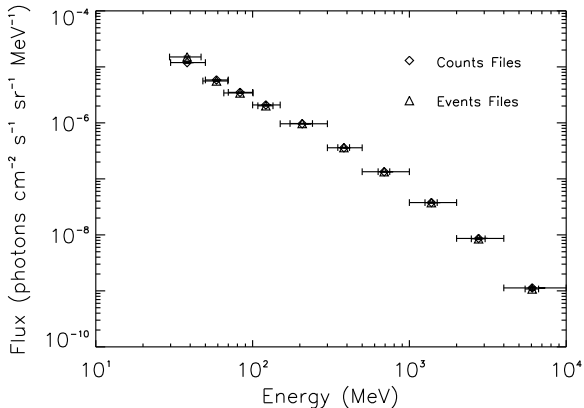


FIG. 1: The differential flux with ten energy bins.

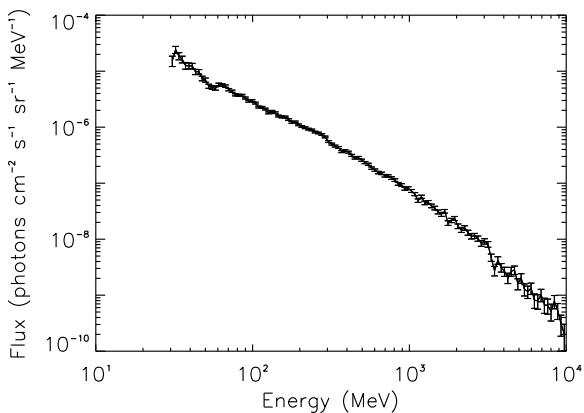


FIG. 2: The photon differential flux using 120 energy bins.

the first source, nuclear interactions, cosmic rays collide with nuclei in interstellar matter to produce neutral pions, which decay mostly into gamma rays [14]. The second process is bremsstrahlung from cosmic-ray electrons interacting with interstellar matter [14]. The third process is inverse-Compton scattering of cosmic-ray electrons with interstellar radiation [14]. The fourth source, interior-point-source emission, comes from unresolved point sources within our Galaxy, such as gamma-ray pulsars [15]. The fifth process, exterior-point-source emission, is produced by unresolved point sources outside our Galaxy such as blazars [16]. Ref. [14] gives the differential gamma-ray production functions for the nuclear and bremsstrahlung contributions. The production functions are for the cosmic-ray spectrum in the solar neighborhood. We assume the production functions at the Galactic center are proportional to the production functions in the solar neighborhood.

These five processes form a continuum background flux of photons upon which the photons from WIMP annihilation are superimposed. Inverse Compton and exterior point sources are subdominant to the other three sources near the Galactic center. We thus model the background from nuclear interactions, bremsstrahlung, and interior point sources, determining the amplitudes of each of these three sources by fitting to the observed flux.

The functional form of the differential flux to which we fitted the data was thus $F(E) = \alpha F_{\text{nuc}}(E) + \beta F_{\text{brem}}(E) + \sigma F_{\text{int}}(E)$, where $F_{\text{nuc}}(E)$, $F_{\text{brem}}(E)$, and $F_{\text{int}}(E)$ are the differential photon fluxes from nuclear interactions, bremsstrahlung, and interior point sources, respectively, and α , β , and σ are amplitudes determined by fitting the data. We use [14] to obtain the source functions

$$F_{\text{nuc}}(E) = \begin{cases} 2.63 \left(\frac{E}{\text{GeV}}\right)^{-2.36} \exp\left[-0.45 \left(\ln\left(\frac{E}{\text{GeV}}\right)\right)^2\right] \text{ cm}^{-2} \text{ s}^{-1} \text{ sr}^{-1} \text{ GeV}^{-1}, & 0.01 \text{ GeV} < E < 1.5 \text{ GeV}, \\ 3.3 \left(\frac{E}{\text{GeV}}\right)^{-2.71} \text{ cm}^{-2} \text{ s}^{-1} \text{ sr}^{-1} \text{ GeV}^{-1}, & 1.5 \text{ GeV} < E < 7.0 \text{ GeV}, \\ 4.6 \left(\frac{E}{\text{GeV}}\right)^{-2.86} \text{ cm}^{-2} \text{ s}^{-1} \text{ sr}^{-1} \text{ GeV}^{-1}, & E > 7.0 \text{ GeV}, \end{cases} \quad (4)$$

$$F_{\text{brem}}(E) = \begin{cases} 0.44 \left(\frac{E}{\text{GeV}}\right)^{-2.35} \text{ cm}^{-2} \text{ s}^{-1} \text{ sr}^{-1} \text{ GeV}^{-1}, & 0.01 \text{ GeV} < E < 5.0 \text{ GeV}, \\ 2.1 \left(\frac{E}{\text{GeV}}\right)^{-3.3} \text{ cm}^{-2} \text{ s}^{-1} \text{ sr}^{-1} \text{ GeV}^{-1}, & 5.0 \text{ GeV} < E < 40 \text{ GeV}. \end{cases} \quad (5)$$

We assume interior point sources to be gamma-ray pulsars. Three pulsars seen by EGRET were the Crab, Geminga, and Vela pulsars, which have photon indices of -2.12 , -1.42 , and -1.62 , respectively [15]. We approximate the photon index as having the average value

of -1.7 , so that

$$F_{\text{int}}(E) = \left(\frac{E}{\text{GeV}}\right)^{-1.7} \text{ cm}^{-2} \text{ s}^{-1} \text{ sr}^{-1} \text{ GeV}^{-1}. \quad (6)$$

The fitted flux $[F_{\text{fit}}(E_i)]$ and the subsequent contributions from each physical process are shown in Fig. 3.

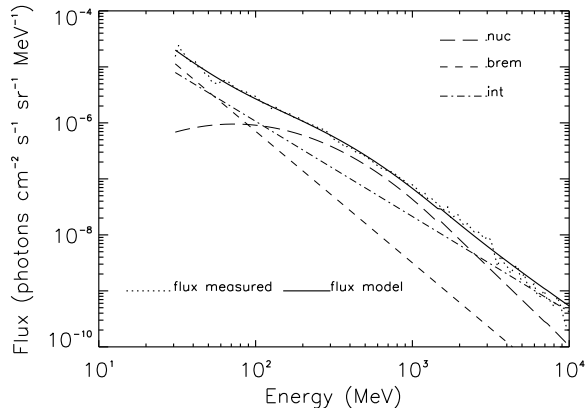


FIG. 3: The measured and model gamma-ray flux along with contributions from nuclear interactions (nuc), bremsstrahlung (brem), and interior point sources (int).

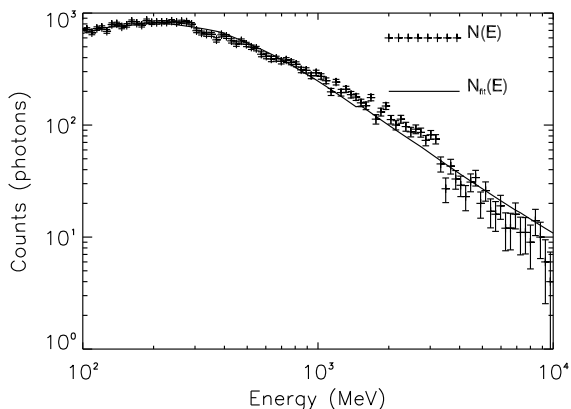


FIG. 4: The spectrum of actual counts, $N(E_i)$, and the fitted spectrum, $N_{\text{fit}}(E_i)$.

V. ANALYSIS OF EXCESS PHOTONS IN GAMMA RAY SPECTRUM

We next construct a residual number of counts by subtracting the fitted number $N_{\text{fit}}(E_i) = F_{\text{fit}}(E_i)\varepsilon(E_i)\Delta E_i$ from the observed number $N(E_i)$ of counts. The counts $N(E_i)$ and $N_{\text{fit}}(E_i)$ are displayed in Fig. 4.

We take the residual spectrum to be the upper limit to the number of photons in each energy bin that could come from WIMP annihilation. However, to search for the signal we must take into account the finite energy resolution. With infinite energy resolution, the WIMP-annihilation excess would appear as a monochromatic peak over a smooth background distribution. However, because of energy uncertainties, each photon captured by EGRET will appear to have an energy equal to its true energy plus an error, which we take to be Gaussian.

TABLE III: Dimensionless resolution R of EGRET at various energies.

Energy (MeV)	R
100	9.42
200	11.21
500	12.39
1000	12.08
3000	11.49
10000	9.07

Thus, monochromatic photons will be spread over neighboring energy bins. Because our bins are logarithmically spaced, the Gaussian will appear skewed, but it will still be distinguishable from the background spectrum.

Suppose our true spectrum before measurement consists of a continuum $C(E_i)$ produced by background radiation and an excess N_p of photons with energy E_p . After measurement, the continuum will change shape but remain smooth, while the excess will spread out as a Gaussian profile over multiple bins. The Gaussian skews negligibly, so we approximate the excess as a standard Gaussian. Thus, we model the data $D(E_i)$ as

$$D(E_i) = C(E_i) + N_p f_p(E_i), \quad (7)$$

where $f_p(E_i)$ is a normalized Gaussian of the form,

$$f_p(E_i) = \frac{\exp\left[-(E_i - E_p)^2/2\sigma_{E_p}^2\right]}{\sum_l \exp\left[-(E_l - E_p)^2/2\sigma_{E_p}^2\right]}. \quad (8)$$

In Eq. (8), the denominator is summed over all energy bins within $3\sigma_{E_p}$ of the Gaussian central energy E_p . The energy uncertainty σ_{E_p} at energy E_p , is given by

$$\sigma_{E_p} = \frac{E_p}{R(E_p)}, \quad (9)$$

where $R(E_p)$ is the dimensionless resolution at energy E_p . The fractional full width at half-maximum (% FWHM), or $\sqrt{2\ln 2}$ times twice the reciprocal of the resolution, is shown for various energies in Fig. 20 in Ref. [11]. From the % FWHM, we produce a table of resolution vs. energy, shown in Table III. We calculate the resolution at each energy by interpolating $\log[R(E)]$ over $\log(E)$. Because the first value for R given in Table III is for energy $E = 100$ MeV, we cannot extrapolate $\log(R)$ to lower energies with certainty. Therefore, we restrict our analysis to the energy interval 0.1 GeV–10 GeV.

The number $N_p(E_i)$ can be deduced at each energy bin in the spectrum by solving Eq. (7) for N_p , assuming $D(E_i)$, $C(E_i)$, and $f_p(E_i)$ are known. Each $N_p(E_i)$ has an uncertainty,

$$\sigma_{N_p}(E_i) = \frac{\sqrt{C(E_i)}}{f_p(E_i)}, \quad (10)$$

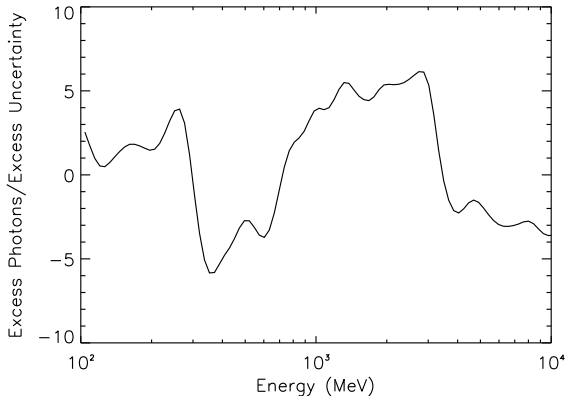


FIG. 5: Ratio of excess photons to the excess uncertainty.

due to continuum fluctuations. Most bins in the spectrum contain large numbers of photons. Therefore, we average N_p using gaussian statistics to calculate \overline{N}_p and $\sigma_{\overline{N}_p}$, the value and uncertainty of the excess, for each energy bin E_p greater than 100 MeV. The resulting ratio of \overline{N}_p to $\sigma_{\overline{N}_p}$ is shown in Fig. 5.

Fig. 5 does show statistically significant deviations of the data from our model for the continuum. To determine if this residual favors the Gaussian model, we compare χ^2 for a Gaussian model to χ^2 for a constant-excess model. We calculate χ^2 for both models over a $\pm 3\sigma_{E_p}$ range centered at the excess center. The Gaussian is $\overline{N}_p f_p$. We also compare the residual with a constant excess N_c , where dN_c/dE is constant and N_c is proportional to the energy-bin size. We normalize N_c such that the lowest energy bin $3\sigma_{E_p}$ from the Gaussian center has 10 photons. We compared χ^2 for the excess at energies $E = 210$ MeV and $E = 2000$ MeV, two energies that have high excess photons to excess uncertainty ratios (see Fig. 5). At both energies we found χ^2 to be smaller for the constant excess, a simpler model, than for the Gaussian. Thus, we show that the residual does not favor the Gaussian model, and we do not attribute any of these deviations to a WIMP-annihilation line (see Fig. 6). Rather, it appears that there is some continuum contribution that our analysis has not taken into account.

We therefore use \overline{N}_p to calculate an upper limit to the line flux. This line flux is different from the differential flux used in previous sections in that this flux is not divided by the energy bin size. Since \overline{N}_p has positive and negative values, we take the 2σ upper limit to the line flux $\Phi_u(E_p)$ to be

$$\Phi_u(E_p) = \begin{cases} (\overline{N}_p + 2\sigma_{\overline{N}_p})/\varepsilon(E_i), & \overline{N}_p \geq 0, \\ 2\sigma_{\overline{N}_p}/\varepsilon(E_i), & \overline{N}_p < 0. \end{cases} \quad (11)$$

The 2σ upper limit to the line flux is shown in Fig. 7.

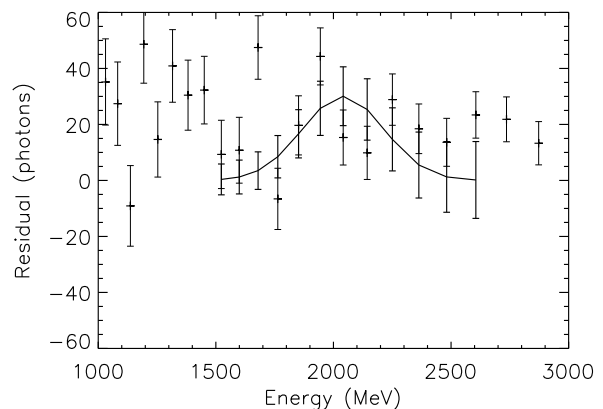
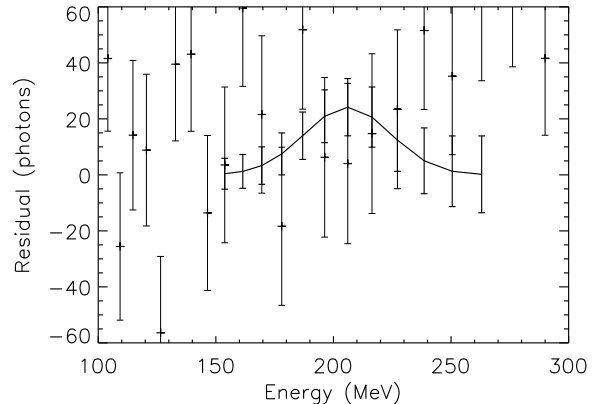


FIG. 6: The residual number of counts (crosses) and the expected Gaussian (solid curve) from a smeared line excess. The top panel shows the residual and Gaussian at $E = 210$ MeV, while the bottom panel shows the same at $E = 2000$ MeV. The ratio of excess photons to excess uncertainty is high at these energies. Notice in both panels the residual does not resemble the Gaussian. For $E = 210$ MeV and $E = 2000$ MeV, respectively, χ^2 for the Gaussian is 17.3 and 38.0 and χ^2 for the constant excess is 11.0 and 23.9. Thus, the Gaussian model is not favored.

VI. UPPER LIMITS TO THE ANNIHILATION CROSS SECTION

If WIMPs comprise the Galactic halo, then the flux of line photons from WIMP annihilation is (for Majorana WIMPs)

$$\Phi(E_\gamma = m_\chi) = \frac{\langle \sigma v \rangle_{\gamma\gamma}}{4\pi m_\chi^2} \int_{l.o.s} \rho_\chi^2 dl, \quad (12)$$

where Φ is the line flux of photons in units of photons $\text{cm}^{-2} \text{s}^{-1} \text{sr}^{-1}$, $\langle \sigma v \rangle_{\gamma\gamma}$ is the velocity-averaged cross section for the WIMP to annihilate to two photons, m_χ is the WIMP mass (which is equal to the photon energy E_γ), and ρ_χ is the density profile of the WIMP halo.

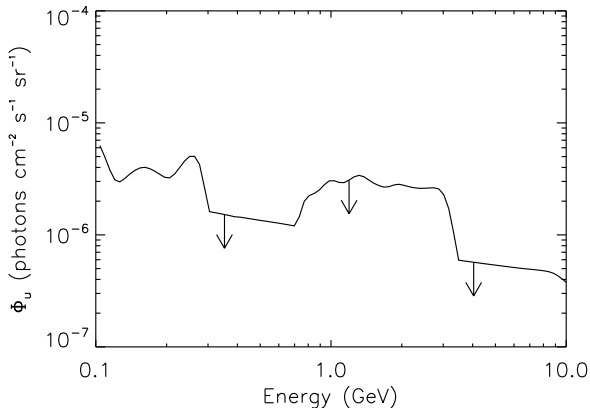


FIG. 7: Upper limit to the line flux Φ_u from the Galactic center.

The integral is along the line of sight, and dl is the differential distance along the line of sight. The residual in the previous Section gives the average line-of-sight line flux within a $10^\circ \times 10^\circ$ region around the Galactic center. Therefore, we integrate Eq. (12) over our viewing region to find the relation between $\langle\sigma v\rangle_{\gamma\gamma}$ and m_χ .

The density profile of the WIMP halo must be known in order to integrate Eq. (12). The functional form of the halo density profile is motivated by theory and simulations, with parameters chosen for consistency with the measured Milky Way rotation curve. We assume the following parametrization of the density profile,

$$\rho(r) = \rho_0 \frac{(r_0/a)^\gamma [1 + (r_0/a)^\alpha]^{(\beta-\gamma)/\alpha}}{(r/a)^\gamma [1 + (r/a)^\alpha]^{(\beta-\gamma)/\alpha}}. \quad (13)$$

Here, ρ_0 is the local density of the halo at the Solar System; r_0 is the distance from the Solar System to the Galactic center, which we take to be 8.5 kpc; a is the core radius; and α , β , and γ are parameters that determine the halo model. Various combinations of α , β , and γ have been used in simulations and are of particular interest. We chose to study the Ka and Kb profiles proposed by Kravtsov et al. [17]; the NFW profile proposed by Navarro, Frenk, and White [10]; and the modified isothermal profile, or Iso, which is commonly used. These profiles are listed in Table IV. The quantities ρ_0 and a are chosen for each profile so that the profile will account for the Galactic rotation curve. These values are taken from Fig. 5 in Ref. [18]. We insert each of these profiles into Eq. (12) and integrate over our viewing region to find the line flux Φ in terms of $\langle\sigma v\rangle_{\gamma\gamma}$ and m_χ .

The resulting upper limit to the annihilation cross section $\langle\sigma v\rangle_{\gamma\gamma}$ is shown in Fig. 8 as a function of WIMP mass m_χ for each halo model listed in Table IV.

TABLE IV: Parameters for each profile type.

Profile	α	β	γ	ρ_0 (GeV/cm ³)	a (kpc)
Ka	2	3	0.2	0.4	11
Kb	2	3	0.4	0.4	12
NFW	1	3	1	0.3	25
Iso	2	2	0	0.3	4

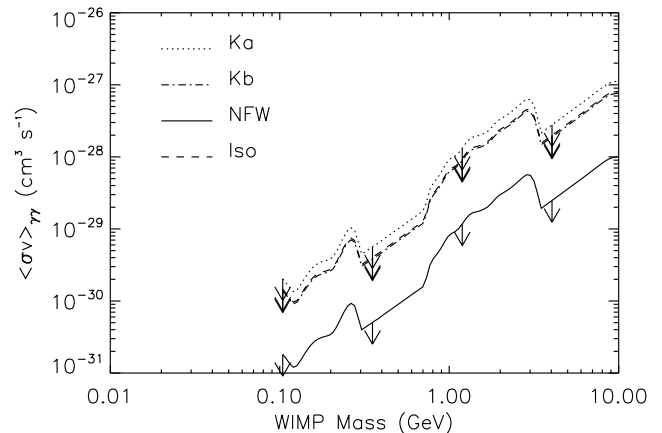


FIG. 8: The 2σ upper limits to the velocity-averaged annihilation cross section $\langle\sigma v\rangle_{\gamma\gamma}$ as a function of WIMP mass for various halo-density profiles.

VII. DISCUSSION

To illustrate the possible utility of this new bound, we consider a toy model in which WIMPs are Majorana fermions that couple to electrons via exchange of a scalar boson (the U boson [19, 20]) of mass m_U (assumed to be much heavier than both WIMPs and electrons) through the Lagrangian density,

$$\mathcal{L} = \frac{C_U f_{Ae}}{2m_U^2} \bar{\chi} \gamma_\mu \gamma_5 \chi \bar{\psi}_e \gamma^\mu \gamma_5 \psi_e, \quad (14)$$

where C_U and f_{Ae} are axial couplings of the U boson to the WIMP field χ and the electron field ψ_e , respectively. Annihilation of WIMPs with $O(\text{MeV})$ masses to electron-positron pairs has been considered as a possible explanation [8] for the observed flux, $\Phi_{511} = 9.9_{-2.1}^{+4.7} \times 10^{-4}$ photons cm⁻² s⁻¹ [21], of 511-keV photons as measured at the Galactic center by the SPI camera on the INTEGRAL satellite. In this scenario, positrons from WIMP annihilation then annihilate with electrons in the IGM to produce these 511-keV photons. The annihilation rate—and therefore the cross section for annihilation to electron-positron pairs and thus the coupling $C_U f_{Ae}/m_U^2$ —are determined by the flux of 511-keV photons. More precisely, the 511-keV flux determines an upper bound to this annihilation rate, cross section, and coupling, but we will here suppose the entire 511-keV flux to be from positrons from WIMP annihilation.

Ref. [22] pointed out that if WIMPs annihilate to electron-positron pairs, they can also undergo annihilation to an electron-positron-photon three-body final state, a process we refer to as internal bremsstrahlung. If $\langle\sigma v\rangle_{e^+e^-}$ is the cross section for annihilation to electron-positron pairs (as calculated, e.g., in Refs. [19, 20, 23]), then the differential cross section for bremsstrahlung of a photon of energy E_γ is

$$\frac{d\langle\sigma v\rangle_{\text{Br}}}{dE_\gamma} = \langle\sigma v\rangle_{e^+e^-} \frac{\alpha_e}{\pi} \frac{1}{E_\gamma} \left[\ln\left(\frac{s'}{m_e^2}\right) - 1 \right] \left[1 + \left(\frac{s'}{s}\right)^2 \right], \quad (15)$$

where $s = 4m_\chi^2$, $s' = 4m_\chi(m_\chi - E_\gamma)$, and α_e is the fine-structure constant. The quantity $E_\gamma^2 d\langle\sigma v\rangle_{\text{Br}}/dE_\gamma$ increases roughly linearly with E_γ for $E_\gamma < m_\chi$ and peaks at a value (for our WIMP mass range of 0.1–10 GeV) less than 10% smaller than the WIMP mass. The measured upper limits to the flux were approximated in Ref. [22] $E_\gamma^2 d\Phi_{\text{Br}}/dE_\gamma \lesssim 7 \times 10^{-3} \text{ MeV cm}^{-2} \text{ s}^{-1} \text{ sr}^{-1}$ over the energy range 1–100 MeV. This flux was averaged over a region on the sky centered at the Galactic center from -30° to 30° Galactic longitude and -5° to 5° Galactic latitude. For the purposes of this illustrative exercise, we extend this bound up to 10 GeV (roughly consistent with the line limit we have derived).

Since each annihilation to an electron-positron pair produces two 511-keV photons, the flux of 511-keV photons is (for Majorana particles)

$$\Phi_{511} = \frac{\langle\sigma v\rangle_{e^+e^-}}{4\pi m_\chi^2} \int \rho_\chi^2 dl d\Omega, \quad (16)$$

where the dl integral is along the line of sight and the $d\Omega$ integral is over the SPI camera's field of view, a 16° -diameter circle around the Galactic center. Likewise, the differential flux of photons from internal bremsstrahlung is

$$\frac{d\Phi_{\text{Br}}}{dE_\gamma} = \frac{d\langle\sigma v\rangle_{\text{Br}}/dE_\gamma}{8\pi m_\chi^2 \Delta\Omega} \int \rho_\chi^2 dl d\Omega, \quad (17)$$

where $\Delta\Omega \simeq 0.182 \text{ sr}$ is the solid angle over the 60° by 10° Galactic region mentioned earlier.

The two-photon annihilation cross section $\langle\sigma v\rangle_{\gamma\gamma}$ for the Lagrangian of Eq. (14) is given by [24]

$$\langle\sigma v\rangle_{\gamma\gamma} = \frac{\alpha_e^2 m_\chi^2 C_U^2 f_{Ae}^2}{\pi^3 m_U^4} |I(\xi_e)|^2, \quad (18)$$

where $\xi_e = m_e^2/m_\chi^2$, $I(\xi_e) = \frac{1}{2} [1 + \xi_e J(\xi_e)]$, and $J(\xi_e)$ is given by

$$J(\xi_e) = \left(\frac{1}{2} \ln \frac{1 + \sqrt{1 - \xi_e}}{1 - \sqrt{1 - \xi_e}} - \frac{i\pi}{2} \right)^2, \quad (19)$$

for $\xi_e \leq 1$. For our WIMP mass range 0.1–10 GeV, $\xi_e \ll 1$ and $I(\xi_e) \simeq 1/2$. The cross section for annihilation to

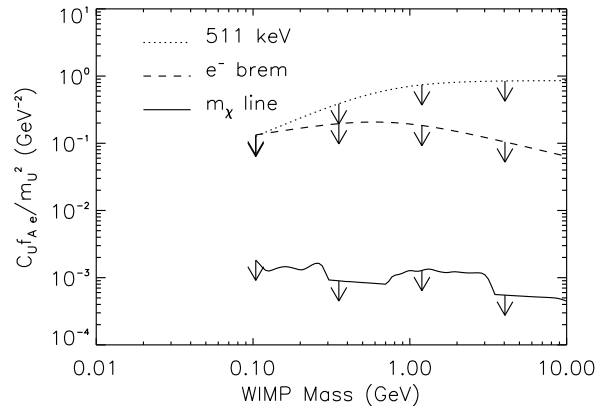


FIG. 9: The 2σ upper limit to the ratio $C_U f_{Ae}/m_U^2$ as a function of WIMP mass for the NFW halo-density profile using the m_χ line with limits using the 511 keV line and internal bremsstrahlung measurements.

electron-positron pairs $\langle\sigma v\rangle_{e^+e^-}$ is given by [20, 23]

$$\langle\sigma v\rangle_{e^+e^-} = \frac{C_U^2 f_{Ae}^2}{2\pi m_U^4} \left[\frac{4}{3} m_\chi^2 \overline{v_\chi^2} + m_e^2 \right], \quad (20)$$

where $\overline{v_\chi^2} = \frac{3}{4} v_c^2$ is the mean-square center-of-mass velocity and $v_c \simeq 220 \text{ km/s}$ is the WIMP rotation speed, assuming the electron energy $E_e = m_\chi \gg m_e$ and $m_U \gg m_\chi$. We use Eqs. (18) and (20) to derive upper limits to the coupling $C_U f_{Ae}/m_U^2$ appearing in the Lagrangian of Eq. (14).

Fig. 9 shows the upper limit, assuming an NFW halo-density profile, to the coupling $C_U f_{Ae}/m_U^2$ from measurements of the 511-keV line [8], the limit to the bremsstrahlung-photon flux [22], and our 2σ limit to the line-photon flux. We see that for the model assumptions and WIMP mass range considered here, the limit to the two-photon annihilation cross section are the strongest of these three. At first, this result may seem surprising, given that the two-photon annihilation process is higher order in α_e , but this suppression is counteracted by the helicity suppression of the cross section for annihilation of Majorana fermions to electron-positron pairs. Refs. [25, 26] considered also gamma-rays from in-flight bremsstrahlung from e^+e^- pairs, but their analysis was restricted to energies $< 100 \text{ MeV}$.

Of course, this conclusion is not model independent, and it may well be that other models—e.g., those in which the dark-matter particle is a scalar [27]—can produce a larger ratio of 511-keV photons to line photons.

Acknowledgments

We thank S. Profumo for useful discussions and comments. ARP was supported by an NSF Graduate Fel-

lowship. RC was partially funded under NASA contract 1407. MK was supported by DoE DE-FG03-92-ER40701,

NASA NNG05GF69G, and the Gordon and Betty Moore Foundation.

-
- [1] L. Bergstrom, Rept. Prog. Phys. **63**, 793 (2000), hep-ph/0002126.
- [2] G. Bertone, D. Hooper, and J. Silk, Phys. Rept. **405**, 279 (2005), hep-ph/0404175.
- [3] G. Jungman, M. Kamionkowski, and K. Griest, Phys. Rept. **267**, 195 (1996), hep-ph/9506380.
- [4] H. E. Haber and G. L. Kane, Phys. Rept. **117**, 75 (1985).
- [5] A. Bottino, F. Donato, N. Fornengo, and S. Scopel, Phys. Rev. **D70**, 015005 (2004), hep-ph/0401186.
- [6] J. F. Gunion, D. Hooper, and B. McElrath, Phys. Rev. **D73**, 015011 (2006), hep-ph/0509024.
- [7] F. Ferrer, L. M. Krauss, and S. Profumo (2006), hep-ph/0609257.
- [8] C. Boehm, D. Hooper, Phys. Rev. Lett. **92**, 101301 (2004), astro-ph/0309686.
- [9] L. Bergstrom and H. Snellman, Phys. Rev. **D37**, 3737 (1988).
- [10] J. F. Navarro, C. S. Frenk, and S. D. M. White, Astrophys. J. **462**, 563 (1996), astro-ph/9508025.
- [11] D. J. Thompson, D. L. Bertsch, C. E. Fichtel, R. C. Hartman, R. Hofstadter, E. B. Hughes, S. D. Hunter, B. W. Hughlock, G. Kanbach, D. A. Kniffen, et al., Astrophys. J. Suppl. **86**, 629 (1993).
- [12] R. C. Hartman et al. (EGRET), Astrophys. J. Suppl. **123**, 79 (1999).
- [13] S. D. Hunter, D. L. Bertsch, J. R. Catelli, T. M. Dame, S. W. Digel, B. L. Dingus, J. A. Esposito, C. E. Fichtel, R. C. Hartman, G. Kanbach, et al., Astrophys. J. **481**, 205 (1997).
- [14] D. L. Bertsch, T. M. Dame, C. E. Fichtel, S. D. Hunter, P. Sreekumar, J. G. Stacy, and P. Thaddeus, Astrophys. J. **416**, 587 (1993).
- [15] J. M. Fierro, P. F. Michelson, P. L. Nolan, and D. J. Thompson, Astrophys. J. **494**, 734 (1998), astro-ph/9709123.
- [16] P. Sreekumar, F. W. Stecker, and S. C. Kappadath, AIP Conf. Proc. **510**, 459 (2004), astro-ph/9709258.
- [17] A. V. Kravtsov, A. A. Klypin, J. S. Bullock, and J. R. Primack, Astrophys. J. **502**, 48 (1998), astro-ph/9708176.
- [18] L. Bergstrom, P. Ullio, and J. H. Buckley, Astropart. Phys. **9**, 137 (1998), astro-ph/9712318.
- [19] C. Boehm and P. Fayet, Nucl. Phys. **B683**, 219 (2004), hep-ph/0305261.
- [20] P. Fayet, Phys. Rev. **D70**, 023514 (2004), hep-ph/0403226.
- [21] P. Jean et al., Astron. Astrophys. **407**, L55 (2003), astro-ph/0309484.
- [22] J. F. Beacom, N. F. Bell, and G. Bertone, Phys. Rev. Lett. **94**, 171301 (2005), astro-ph/0409403.
- [23] H. Goldberg, Phys. Rev. Lett. **50**, 1419 (1983).
- [24] S. Rudaz, Phys. Rev. **D39**, 3549 (1989).
- [25] J. F. Beacom and H. Yuksel, Phys. Rev. Lett. **97**, 071102 (2006), astro-ph/0512411.
- [26] P. Sizun, M. Casse, and S. Schanne, Phys. Rev. **D74**, 063514 (2006), astro-ph/0607374.
- [27] C. Boehm, J. Orloff, and P. Salati (2006), astro-ph/0607437.